9.4 Stereo PIV Applied to a Vortex Ring Flow

Contributed by:
C. Willert

The various methods of image reconstruction and calibration as described in section 7.1 were applied in the measurement of the unsteady vortex ring flow field. Figure 9.18 outlines a vortex ring generator having a simple construction with very reproducible flow characteristics. The vortex ring is generated by discharging a bank of electrolytic capacitors (60 000 μF) through a pair of loudspeakers which are mounted facing inward on to two sides of a wooden box. By forcing the loudspeaker membranes inward, air is impulsively forced out of a cylindrical, sharpened nozzle (inner diameter= 34.7 mm) on the top of the box. The shear layer formed at the tip of the nozzle then rolls up into

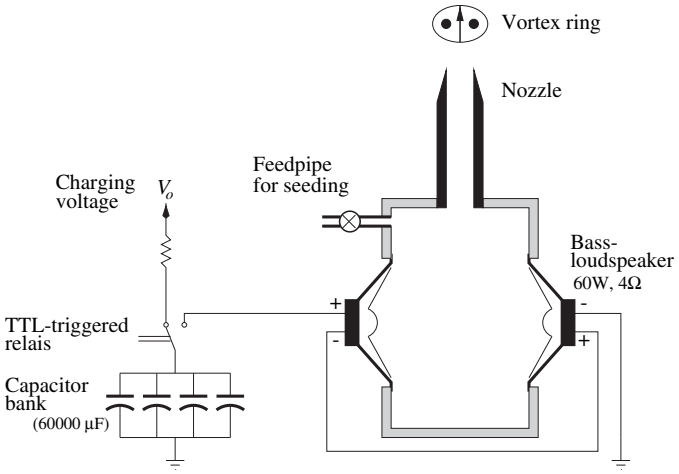

Fig. 9.18. Schematic of the vortex ring generator used to obtain an unsteady, yet reproducible flow field.

a vortex ring and separates from the nozzle as the membranes move back to their equilibrium positions due to the decay in supply voltage. As long as the charging voltage is kept constant, the formation of the vortex ring will be very reproducible. The generator also has a seeding pipe with a check valve allowing the interior of the box and ultimately the core of the vortex ring to be seeded.

9.4.1 Imaging Configuration and Hardware

A noteworthy feature of the imaging configuration outlined in figure 9.19 – which has also been used for the error estimation given in section 7.1 – is that the cameras are positioned on both sides of the light sheet. This arrangement allows both cameras to make use of the much higher forward scattering properties of the small (1 μm) oil droplets used for seeding. The principal viewing axes are both around 35° from the light sheet normal such that the combined opening angle is approximately 70° near the center of the image.

A pair of 100 mm, $f_{\#}$ 2.8 objective lenses constitute the recording optics and are connected to the CCD cameras using specially built tilt-adapters (see figure 9.20). Using a pair of set screws on each of the adapters, the angle between the lens and the sensor (image plane) can be easily and precisely

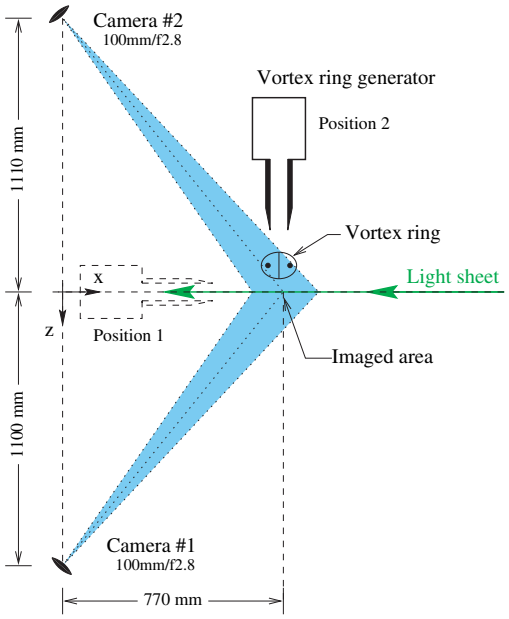

Fig. 9.19. Stereoscopic imaging configuration in forward scattering mode for both cameras.

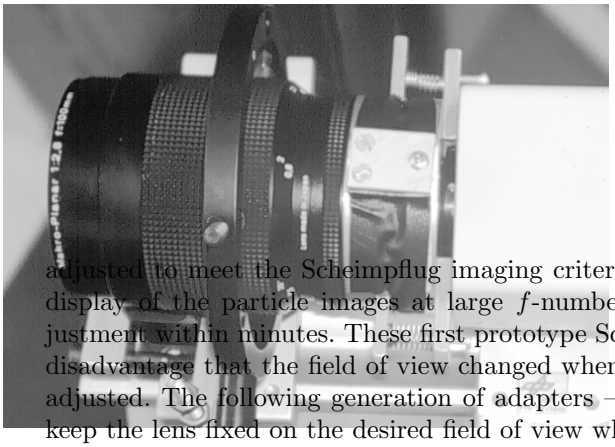

Fig. 9.20. A specially built tilt-adapter between the lens and the sensor allows adjustment according to the Scheimpflug criterion.

adjusted to meet the Scheimpflug imaging criterion (see section 7.1). A live display of the particle images at large f-numbers permits an accurate adjustment within minutes. These first prototype Scheimpflug adapters had the disadvantage that the field of view changed when the Scheimpflug angle was adjusted. The following generation of adapters – now commonly available – keep the lens fixed on the desired field of view while the sensor plane (CCD) is rotated within the plane of focus.

In the imaging arrangement shown in figure 9.19 the Scheimpflug angle (ϕ in figure 7.1b) was measured to be approximately 2.7°. The field of view covered about 145 mm horizontally by 115 mm vertically across the center of the image. The edge loss due to the Scheimpflug imaging arrangement was about 5 mm vertical from side to side, but since both cameras were positioned nearly symmetrically, the field of view could be matched very well, thereby allowing three-dimensional PIV measurements across the entire sensor area. This is an advantage over the "classical" stereoscopic arrangement in which both cameras view from the same side of the light sheet because the non-overlapping areas are of no use in the three-dimensional reconstruction.

The cameras used for this experiment are based on a full frame interline transfer CCD sensor with a 1008H by 1018V pixel resolution. The light sheet was generated by a frequency doubled, double oscillator Nd:YAG laser with more than 300 mJ per pulse. Synchronization between the cameras and the laser was achieved by means of a multiple channel sequencer. Since one of the cameras was not capable of operating in a triggered mode it provided the master timing of the entire PIV recording system. The second was operated in an asynchronously triggered mode. Two separate personal computers with interface cards captured the image pairs from the cameras at a common image pair rate of 5 Hz. (In principle the use of a common PC for both cameras would have also been possible.) One of the computers provided the trigger pulse for the vortex generator as soon as the image acquisition was started. By adding

a time delay (or by moving the vortex generator back and forth) the position of the vortex ring within the PIV recording could be adjusted.

The light sheet thickness was set at approximately 2.5 mm, while the pulse delay was varied within $300 \leq \Delta t \leq 500\,\mu$s with the vortex ring propagating in-line with the light sheet (position 1 in figure 9.19), and $\Delta t = 200\,\mu$s while propagating normal to the light sheet (position 2 in figure 9.19). With maximum velocities of 3.5 m/s this translated to maximum displacements of 0.7 mm for the vortex ring passage normal to the light sheet. Effectively, the loss of pairs was kept to less than 30% thereby ensuring a high data yield even in regions of high out-of-plane motion. The f-number was set to $f_{\#} = 2.8$.

9.4.2 Experimental Results

Initially the nozzle of the vortex ring generator was placed collinearly with the light sheet to provide cross-sectional cuts through the vortex ring (figure 9.21). This provided reference data as well as information on the ring's circulation and stability. In the second configuration, that is, position 2 in figure 9.19, the generator was placed normal to the light sheet. Figure 9.22 shows a pair of two-component velocity fields prior to their combination into a three-component data set. The stereoscopic view is clearly visible. Stereoscopic reconstruction using equation (7.3), equation (7.5) and equation (7.8) then produces the desired three-component data set of figure 9.23.

In terms of processing, the image back projection was chosen such that the magnification factor was constant at $10\,\text{pixel}\,\text{mm}^{-1}$ in all images after recon-

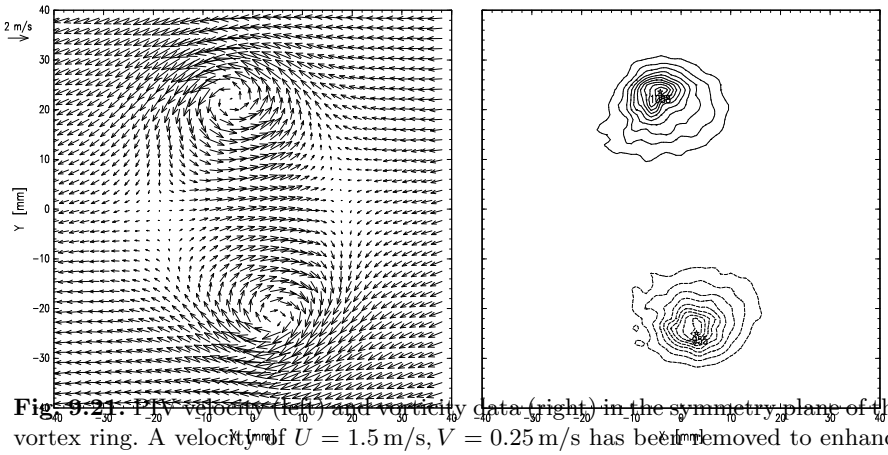

Fig. 9.21. PIV velocity (left) and vorticity data (right) in the symmetry plane of the vortex ring. A velocity of $U = 1.5\,\text{m/s}, V = 0.25\,\text{m/s}$ has been removed to enhance the visibility of the flow's features. The propagation of the ring is left to right and slightly upward (the nozzle was inclined with the horizontal). The vorticity contours are spaced in intervals of $100\,\text{s}^{-1}$ excluding 0.

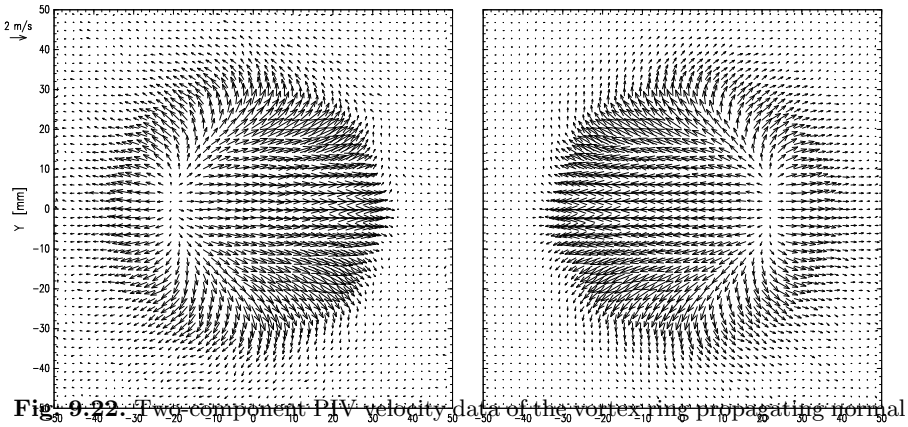

Fig. 9.22. Two-component PIV velocity data of the vortex ring propagating normal to the light sheet as viewed by camera 1 (left) and camera 2 (right).

struction. The final image size of 1450 horizontal by 1200 vertical pixel is about 70% larger than the original images. An interrogation area of 32×32 pixel with an overlap (oversampling) of 66% was chosen although only every fourth vector is shown in the plots (i.e. 33% overlap). In physical space the interrogation window covers $3.2 \times 3.2\,\mathrm{mm}^2$ while the grid spacing is $1.0 \times 1.0\,\mathrm{mm}^2$. The particle image density was high enough to achieve valid data rates exceeding 99% over the entire field of view. It was also found that image preconditioning

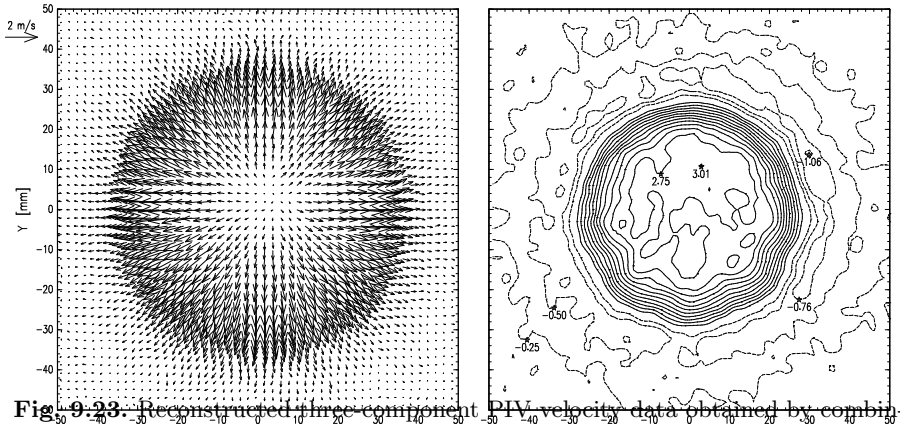

Fig. 9.23. Reconstructed three-component PIV velocity data obtained by combining the data sets shown in figure 9.22. The out-of-plane velocity component w is shown as a contour plot on the right (contour levels at 0.25 m/s).

– adaptive background subtraction using a 7×7 pixel kernel highpass filter and subsequent binarization – significantly improved the data yield by bringing most particle images to the same intensity level.

After the displacement estimation automated outlier detection found of the order of 100 outliers per 16 600 vector data set. Most of these were found on the edges of the original image domain outside of which particle images do not exist. Only very few outliers (< 10) were detected in the central 95% of the field of view, especially in regions of high gradients. The detected outliers were then linearly re-interpolated to allow a subsequent three-dimensional reconstruction.